Monte Carlo study of the symmetric Anderson-impurity model

R. M. Fye and J. E. Hirsch
Department of Physics, University of California, San Diego, La Jolla, California 92093
(Received 13 November 1987)

Using a recently proposed quantum Monte Carlo technique, we consider moment formation and magnetic properties of the symmetric Anderson-impurity model for a wide range of parameters and temperatures. We parametrize the general behavior, determining the approach towards universality and establishing the range of validity of various approximations.

I. INTRODUCTION

The Anderson-impurity Hamiltonian,[1]

$$H=\sum_{\mathbf{k},\sigma}\varepsilon_{\mathbf{k}}c^{\dagger}_{\mathbf{k}\sigma}c_{\mathbf{k}\sigma}+\sum_{\mathbf{k},\sigma}V_{\mathbf{k}}(c^{\dagger}_{\mathbf{k}\sigma}d_{\sigma}+d^{\dagger}_{\sigma}c_{\mathbf{k}\sigma})+\varepsilon_d\sum_{\sigma}n_{d\sigma}+Un_{d\uparrow}n_{d\downarrow}\ , \tag{1}$$

has been widely used to describe impurity magnetic properties in metals. In this Hamiltonian, the $c_{\mathbf{k}\sigma}$'s refer to conduction-electron states; the d_{σ}'s refer to impurity states; the $\varepsilon_{\mathbf{k}}$'s are conduction-electron energies; the $V_{\mathbf{k}}$'s refer to hybridization between conduction-electron and impurity states; ε_d is the energy of a singly occupied impurity level; U refers to the Coulomb repulsion between two opposite-spin impurity electrons; and we assume that the impurity states have no orbital degeneracy. We will consider in this paper the particle-hole-symmetric case of this model, $\varepsilon_d+\frac{1}{2}U=0$, which is the most favorable for the formation of an impurity magnetic moment. Through the use of the Schrieffer-Wolff transformation,[2] which maps the Anderson impurity into a Kondo spin-impurity model, we expect similar results for the case of a well-developed impurity moment or for the almost-symmetric case.

The impurity magnetic susceptibility properties of the Anderson Hamiltonian have been explored numerically by renormalization-group techniques at finite temperature[3] and by Bethe-ansatz techniques at zero temperature and numerically at finite temperatures.[4–6] However, the formation of the impurity moment has not been quantitatively considered using either technique, and only a limited number of finite-temperature susceptibility graphs have been published.[3,6] It is thus the purpose of this paper to explore and parametrize the local-moment formation and susceptibility properties of the Anderson-impurity model in more detail than has previously been done.

We begin by discussing a recently proposed Monte Carlo technique[7] which gives essentially exact results for interacting impurity systems. We then present magnetic susceptibility and local-moment results for a wide range of parameters, comparing our data with the universal Kondo curve and also with high-temperature perturbative expansions. We next consider the maximum values of the local moment and of the "effective moment" $T\chi$, where χ is the impurity magnetic susceptibility, and compare them with zero-temperature Hartree-Fock predictions. Lastly, we consider the effect of band structure on local-moment development, and conclude with a discussion and summary.

II. TECHNIQUE

We will discuss the technique as applied to the single-impurity Anderson model, although it is generally applicable to any system of electrons where part of the degrees of freedom describe interacting electrons and part noninteracting ones. It is also applicable in the limit where all electrons interact, as the single-band Hubbard model, although in that case it is usually less efficient than a related approach developed by Blankenbecler, Scalapino, and Sugar (BSS).[8] The basic idea of our approach is that in the Monte Carlo simulation it is sufficient to keep track of only the Green's function for the interacting degrees of freedom, provided its full imaginary-time dependence is kept. Conversely, in the BSS approach the Green's function for all degrees of freedom is needed (interacting and noninteracting), but only for equal times.

We write the single-impurity Anderson Hamiltonian as

$$H=H_0+H_1\ , \tag{2}$$

where

$$H_0=\sum_{\mathbf{k},\sigma}\varepsilon_{\mathbf{k}}c^{\dagger}_{\mathbf{k}\sigma}c_{\mathbf{k}\sigma}+\sum_{\mathbf{k},\sigma}V_{\mathbf{k}}(c^{\dagger}_{\mathbf{k}\sigma}d_{\sigma}+\text{H.c.})+\left[\varepsilon_d+\frac{U}{2}\right]\sum_{\sigma}n_{d\sigma} \tag{3}$$

and

$$H_1=U[n_{d\uparrow}n_{d\downarrow}-\tfrac{1}{2}(n_{d\uparrow}+n_{d\downarrow})]\ . \tag{4}$$

More generally, H_0 would contain only bilinear terms in the Hamiltonian, and H_1 all interaction terms. We write the partition function as[9]

$$Z=\mathrm{Tr}e^{-\beta H}=\mathrm{Tr}\left[\prod_{l=1}^{L}e^{-\Delta\tau(H_0+H_1)}\right]\cong\mathrm{Tr}\left[\prod_{l=1}^{L}e^{-\Delta\tau H_0}e^{-\Delta\tau H_1}\right]\ , \tag{5}$$

with $\Delta\tau=\beta/L$. The interaction terms in H_1 are then eliminated by introducing auxiliary Ising variables[10]

$$\exp\{-\Delta\tau U[n_\uparrow n_\downarrow-\tfrac{1}{2}(n_\uparrow+n_\downarrow)]\} = \tfrac{1}{2}\mathrm{Tr}_\sigma\{\exp[\lambda\sigma(n_\uparrow-n_\downarrow)]\} , \quad (6)$$

where $\cosh\lambda=\exp(\Delta\tau U/2)$. This brings the Hamiltonian to bilinear fermion form in a τ-dependent $\{\sigma_l\}$ field, where $\tau_l=l\Delta\tau$.

Taking the trace over the fermion degrees of freedom then yields

$$Z=\mathrm{Tr}_{\{\sigma_l\}}\left[\prod_{\mu=\pm1}\det{}_{N,L}\mathcal{O}_\mu[\{\sigma_l\}]\right] , \quad (7)$$

where $\mathcal{O}_\mu$ is an $NL\times NL$ matrix, with N the number of spatial sites (or k vectors) for the conduction electrons plus 1 for the impurity orbital. Written out in the time direction, $\mathcal{O}_\mu$ is

$$\mathcal{O}_\mu=\begin{pmatrix} I & 0 & 0 & \cdots & e^{-(\Delta\tau)K} & e^{V_L^\mu} \\ -e^{-\Delta\tau K}e^{V_1^\mu} & I & 0 & & & \\ 0 & -e^{-\Delta\tau K}e^{V_2^\mu} & I & & & \\ & & \ddots & & & \\ & & & \ddots & & \\ & & & & \ddots & \end{pmatrix} , \quad (8)$$

where K is an $N\times N$ matrix for the bilinear part of H,

$$H_0=\sum_{\substack{i,j\\ \sigma}} a_{i\sigma}^\dagger K_{ij}a_{j\sigma} , \quad (9)$$

with $a_{i\sigma}$ denoting c or d operators, and i,j running over all orbital degrees of freedom; and

$$V_l^\mu=\lambda\mu\sigma_l\,|\,d\,\rangle\langle\,d\,| \quad (10)$$

is a potential acting only at the impurity site. More generally, in a problem involving n interacting degrees of freedom, V_l^μ would be an $n\times n$ matrix.

For both the Monte Carlo updating and the evaluation of observables we will need the Green's function, defined by

$$g^\mu=\mathcal{O}_\mu^{-1} . \quad (11)$$

Given two arbitrary Ising configurations giving rise to potentials V and V' (we omit μ indices for simplicity), the Green's function obeys the Dyson equation

$$g'=g+(g-I)(e^{V'-V}-I)g' \quad (12a)$$

and its transpose

$$g'=g+(g'-I)(I-e^{-V'+V})g . \quad (12b)$$

Equation (12) is most easily established by first finding the Dyson equation for

$$\tilde{g}=e^V g , \quad (13)$$

i.e.,

$$\tilde{g}=\begin{pmatrix} e^{-V_1} & 0 & & \\ -e^{-\Delta\tau K} & e^{-V_2} & 0 & \\ & \ddots & \ddots & \end{pmatrix}^{-1} . \quad (14)$$

Its Dyson equation

$$\tilde{g}'=\tilde{g}-\tilde{g}(e^{-V'}-e^{-V})\tilde{g}' \quad (15)$$

follows simply from the matrix identity

$$1/(A+B)=1/A-(1/A)B[1/(A+B)] ,$$

and Eq. (12) follows by substitution.

Note that we may use Eq. (12) as a matrix equation for all components of g at the impurity site (or sites in a more general case) only,

$$g'_{dd}=g_{dd}+(g_{dd}-I)(e^{V'-V}-I)g'_{dd} , \quad (16)$$

where g_{dd} is an $L\times L$ matrix. Given g_{dd} for a configuration with potential V, we can obtain the impurity Green's function for a configuration V' by inverting an $L\times L$ matrix,

$$g'_{dd}=[I-(g_{dd}-I)(e^{V'-V}-I)]^{-1}g_{dd} . \quad (17)$$

Similarly, we can obtain the Green's function for arbitrary sites for a potential V' if we know it for the potential V and we also know g'_{dd} from Eq. (17),

$$g'_{cd}=g_{cd}+g_{cd}(e^{V'-V}-I)g'_{dd} , \quad (18a)$$

$$g'_{dc}=g_{dc}+(g'_{dd}-I)(I-e^{-V'+V})g_{dc} , \quad (18b)$$

$$g'_{cc'}=g_{cc'}+g_{cd}(e^{V'-V}-I)g'_{dc'} . \quad (18c)$$

Initially, we find the Green's functions in the absence of impurity potential ($U=0$) by standard techniques. For the single-impurity symmetric Anderson model, the impurity Green's function is

$$g^0_{dd}(l,l')=\frac{1}{\beta}\sum_n e^{-i\omega_n(\Delta\tau)(l-l')}g^0_{dd}(i\omega_n) \quad (19)$$

and

$$g^0_{dd}(i\omega_n)=-\frac{1}{i\omega_n-V^2\sum_k\frac{1}{i\omega_n-\varepsilon_k}} , \quad (20)$$

with $\omega_n=(2n+1)\pi/\beta$. As in most previous work, we assume that V_k is independent of k and that the conduction band has a constant single-particle density of states ρ. For an infinite conduction band,

$$g^0_{dd}(i\omega_n)=-\frac{1}{i\omega_n-i\Delta\,\mathrm{sgn}(\omega_n)}\ , \tag{21}$$

where $\Delta=\pi\rho V^2$ is the half width at half maximum of the impurity state caused by impurity-conduction hybridization. We also treat moment formation for the case of finite conduction bandwidth D.

We next compute the impurity Green's function in the presence of an initial potential (chosen, for example, randomly) from Eq. (17). The Monte Carlo procedure then consists of attempting to flip sequentially the Ising spins, and accepting or rejecting the move using the standard Metropolis algorithm. Under a proposed change $\sigma_l\rightarrow\sigma_l'=-\sigma_l$, the ratio of determinants between the new and old configurations is given by[8]

$$R_\mu=\frac{\det(\mathcal{O}_\mu[\sigma_l'])}{\det(\mathcal{O}_\mu[\sigma_l])}=1+[1-g^\mu_{dd}(l,l)](e^{V_l'^\mu-V_l^\mu}-1)\ , \tag{22}$$

as can be easily found using $\tilde{g}$, Eq. (15). Because of particle-hole symmetry, the product $R=R_+R_-$ is always positive in the symmetric Anderson model. If R is greater than a number between 0 and 1 randomly selected, the move is accepted; otherwise, it is rejected. If the move is accepted, all time components of the impurity Green's function for the new configuration are obtained from the old through the relation

$$g'_{dd}(l_1,l_2)=g_{dd}(l_1,l_2)+[g_{dd}(l_1,l)-\delta_{l_1,l}](e^{V_l'-V_l}-1)\left[\frac{1}{1+[1-g_{dd}(l,l)](e^{V_l'-V_l}-1)}\right]g_{dd}(l,l_2)\ , \tag{23}$$

which follows directly from Eq. (12).

To summarize, for the Monte Carlo updating we need to know the Green's function at the space and time site of the field being updated. In the present procedure, we keep all time components of the Green's function at the impurity site, which are continuously updated through Eq. (23). Thus each updating involves L^2 operations (n^2L^2 for n impurities). Alternatively, in the BSS algorithm all equal-time components of the Green's function are used for the updating (at all N interacting and noninteracting sites), so that an updating involves N^2 operations. Clearly, as far as computer time is concerned, the present approach wins only for problems with relatively few interacting sites compared to noninteracting ones. However, it turns out that the present approach is *stable* at low temperatures while in the BSS approach instabilities appear that prevent one from going to very low temperatures. This different behavior is related to the different eigenvalue structure of the space and time Green's functions.

To compute observables, we use the fact that Wick's theorem applies due to the bilinear form of Eq. (5) when Eq. (6) is used. We measure the local moment

$$\langle\sigma_z^2\rangle=\langle(n_{d\uparrow}-n_{d\downarrow})^2\rangle \tag{24}$$

and the impurity magnetic susceptibility in the z and x directions

$$\chi_z=\Delta\tau\sum_{l=0}^{L-1}\langle[n_{d\uparrow}(\tau_l)-n_{d\downarrow}(\tau_l)][n_{d\uparrow}(0)-n_{d\downarrow}(0)]\rangle \tag{25}$$

and

$$\chi_x=\Delta\tau\sum_{l=0}^{L-1}\langle[d^\dagger_\uparrow(\tau_l)d_\downarrow(\tau_l)+d^\dagger_\downarrow(\tau_l)d_\uparrow(\tau_l)]\times[d^\dagger_\uparrow(0)d_\downarrow(0)+d^\dagger_\downarrow(0)d_\uparrow(0)]\rangle\ , \tag{26}$$

which should be identical from rotational invariance. Using the two different definitions of χ allows us to pick the one with less statistical error, and also to check for statistical error consistency.

For both $\langle\sigma_z^2\rangle$ and for $T\chi_z$ and $T\chi_x$, the error due to the Trotter approximation of Eq. (5) is proportional to $(\Delta\tau)^2$ for $\Delta\tau$ sufficiently small, and remains finite as $T\rightarrow0$.[11,12] Thus for each temperature and set of parameters, we take measurements for smaller and smaller values of $\Delta\tau$ and plot these results versus $(\Delta\tau)^2$, until we have reached the error regime linear in $(\Delta\tau)^2$. We then extrapolate to the exact $\Delta\tau=0$ limit. This procedure has allowed us to study larger U and, hence, greater moment formation than previous Monte Carlo studies.[7,13,14]

We show three sample graphs of $(\Delta\tau)^2$ extrapolation in Figs. 1–3. Figures 1 and 2 illustrate a "worst-case" extrapolation (i.e, large U and β). Figure 3 illustrates a more representative case for $T\chi$.

As a test of the algorithm, we made extensive comparisons of Monte Carlo and exact diagonalization results for an impurity on a two-site lattice. We also computed Monte Carlo calculations with renormalization-group results; as can be seen in Fig. 4, agreement is quite good.

III. FINITE-TEMPERATURE BEHAVIOR FOR INFINITE CONDUCTION BAND

A. $T\chi$

We show in Fig. 5 $T\chi$ versus $\log_2$ for $\Delta=\frac{1}{2}$ and $U=0$, 1, 1.5, 2, 3, 4, 6, 8, 12, and 16 for the case of a flat conduction-band density of states of infinite width. We also show on the same graph the corresponding universal Kondo curves,[15] with Kondo temperatures $T_k=0.324$, 0.169, 0.121, 0.0867, 0.0436, 0.0216, 5.18×10^{-3}, 1.20×10^{-3}, 6.16×10^{-5}, and 3.02×10^{-6}. The Kondo temperature is obtained from the Bethe-ansatz formula[4,16]

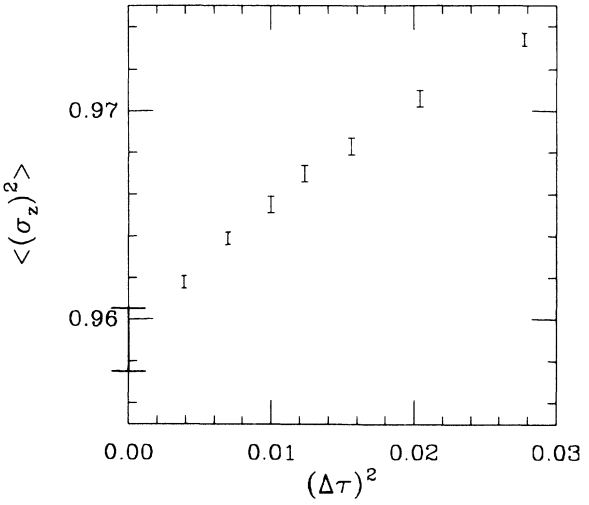

FIG. 1. Local moment $\langle \sigma_z^2 \rangle$ vs $(\Delta\tau)^2$ for $U=8$, $\Delta=\frac{1}{2}$, and $\beta=8$, showing extrapolation.

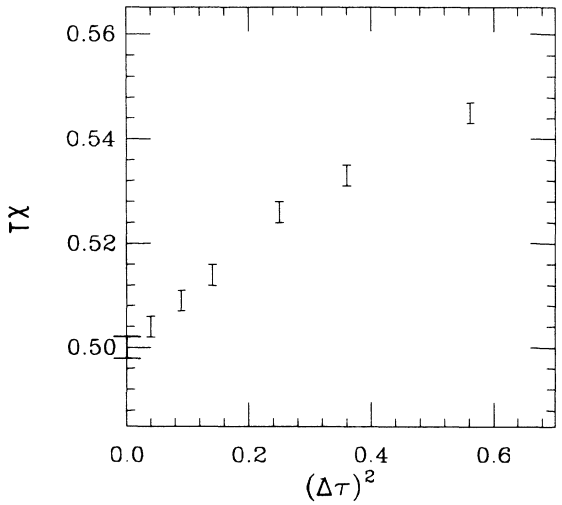

FIG. 3. $T\chi$ vs $(\Delta\tau)^2$ for $U=3$, $\Delta=\frac{1}{2}$, and $\beta=6$, showing extrapolation.

$$T_k=\frac{0.103}{\chi(T=0)}\ , \tag{27}$$

$$\chi(T=0)=\chi_k\left[1+\frac{1}{\sqrt{\pi}}\int_0^{1/2u}\frac{dx}{\sqrt{x}}\exp\left[x-\frac{\pi^2}{16x}\right]\right]\ , \tag{28}$$

and

$$\chi_k=\frac{1}{2\pi\Delta}\left[\frac{\pi}{2u}\right]^{1/2}\exp\left[\frac{\pi^2 u}{8}-\frac{1}{2u}\right]\ , \tag{29}$$

with $u=U/\pi\Delta$. In the noninteracting limit

$$\lim_{U\to 0} T_k=(0.647)\Delta\ . \tag{30}$$

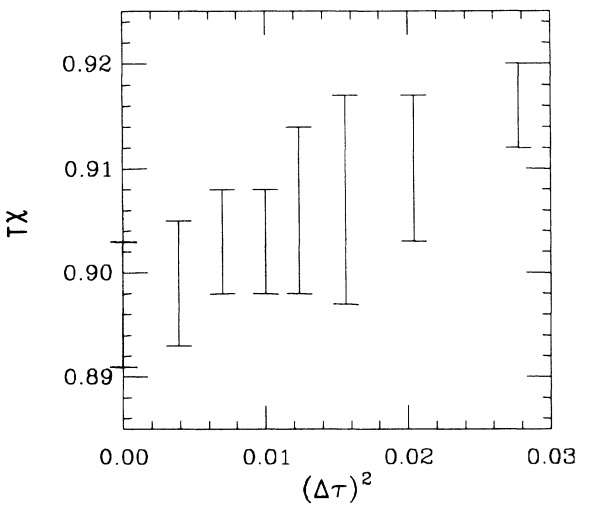

FIG. 2. $T\chi$ vs $(\Delta\tau)^2$ for $U=8$, $\Delta=\frac{1}{2}$, and $\beta=8$, showing extrapolation.

In the opposite limit, $U\gg\Delta$, T_k can be written in the Kondo-like form[15]

$$T_k\approx D_{\rm eff}(\rho J)^{1/2}e^{-(1/\rho J)}\ , \tag{31}$$

where

$$\rho J=\frac{8\Delta}{\pi U} \tag{32}$$

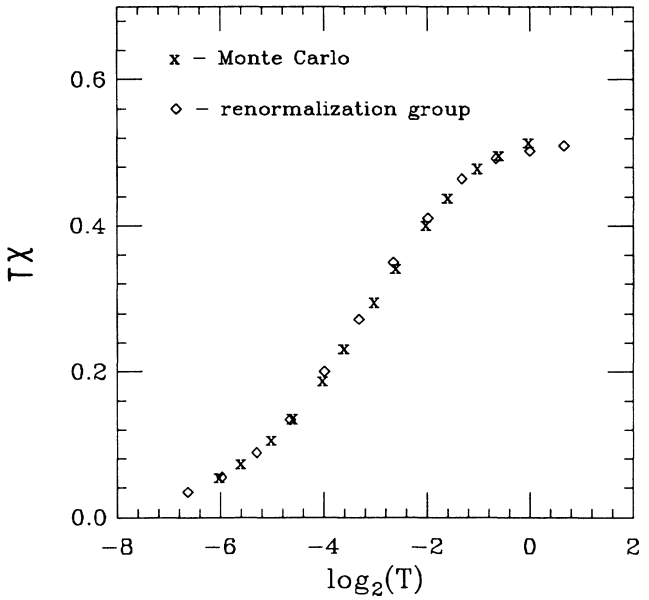

FIG. 4. Monte Carlo and renormalization-group results for $T\chi$ with $U/\pi\Delta=1.013$. Renormalization-group data points are taken from Fig. 9 of Ref. 3 and normalized to $\Delta=\frac{1}{2}$ for direct comparison with the Monte Carlo results. $D=\infty$ for the Monte Carlo points; $D=10^3U=1.591\times10^3$ for the renormalization-group points. Estimated Monte Carlo errors are less than or equal to symbol size.

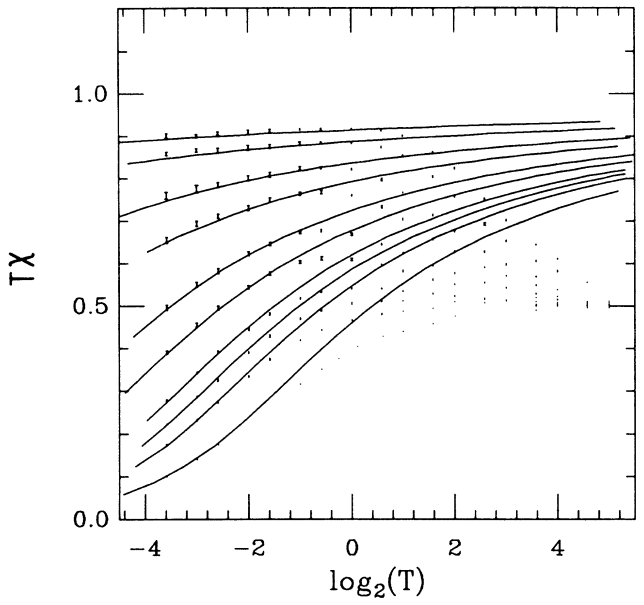

FIG. 5. $T\chi$ vs $\log_2(T)$ for $\Delta=\frac{1}{2}$ and $U=0$, 1, 1.5, 2, 3, 4, 6, 8, 12, and 16. Solid lines are universal Kondo curves with T_k computed from the Bethe-ansatz formula (i.e., no free parameters).

and[17]

$$D_{\text{eff}}=(0.182)U \ . \tag{33}$$

In Fig. 6, we plot the same Monte Carlo results as in Fig. 5, but compare them rather with the high-T perturbations series of Haldane,[17]

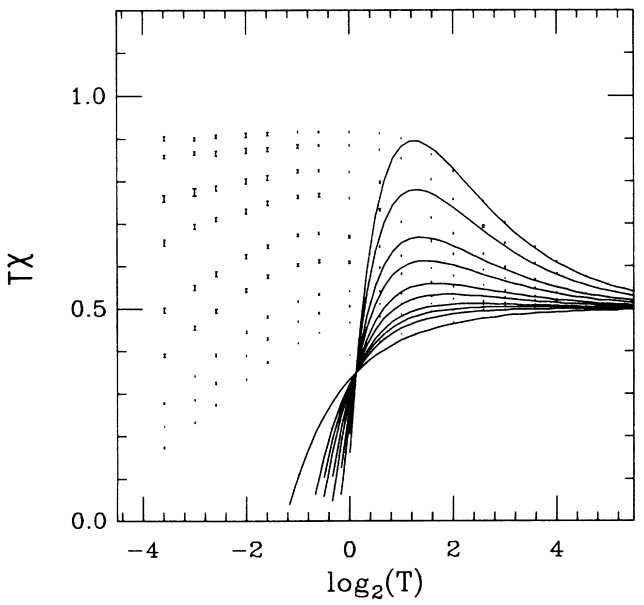

FIG. 6. Same data points as Fig. 5. Solid lines are from a high-temperature perturbative expansion of $T\chi$ through order β^2.

$$T\chi \approx \frac{1}{2}+\frac{1}{T}\left[\frac{U}{8}-A\left[\frac{\Delta}{\pi}\right]\right] -\frac{1}{T^2}\left[AU\left[\frac{\Delta}{\pi}\right]+\frac{B}{2}\left[\frac{\Delta}{\pi}\right]^2\right], \tag{34}$$

where $A=0.853$ (Ref. 17) and $B=2.45\pm0.10$ was determined using our algorithm for $U=0$.

Thus, we see that, for all U studied, $T\chi$ is well described by Eq. (34) down to $T\sim20\Delta$, where it begins to move towards the corresponding Kondo curve. It joins the Kondo curve at $T_j\sim\frac{1}{3}\Delta$ for $U=0$; for $U>\pi\Delta$, our results suggest $T_j\sim\frac{1}{4}\sqrt{\Delta U}$, though other functional dependences are not ruled out. This latter formula is in general agreement with Bethe-ansatz conditions,[5] which predict Kondo-like behavior for $U\gg\Delta$ and $T\ll\sqrt{\Delta U}$. For $U>2\pi\Delta$, $T\chi$ reaches its maximum when it joins the universal curve at T_j; for $U<2\pi\Delta$, the maximum is reached at a temperature above T_j.

Our graphs for $T\chi$ (as well as those of other publications[3,6]) either monotonically decrease or monotonically increase and then monotonically decrease as the temperature is lowered. Thus, using Eq. (34), we see that there is a crossover behavior in the "effective moment" $T\chi$ at

$$U_c=(2.17)\Delta \ , \tag{35}$$

such that $(T\chi)_M>0.5$ for $U>U_c$ and $(T\chi)_M=0.5$ for $U\le U_c$, where $(T\chi)_M$ is the maximum value of $T\chi$. This is reminiscent of the Hartree-Fock critical value for moment formation[1]

$$U_c=\pi\Delta \ . \tag{36}$$

However, it is much closer to the Bethe-ansatz value[5]

$$U_c=2\Delta \ , \tag{37}$$

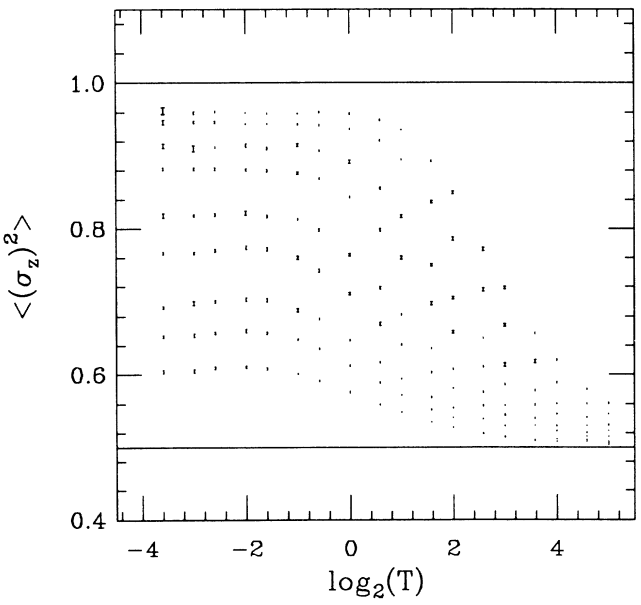

FIG. 7. $\langle\sigma_z^2\rangle$ vs $\log_2(T)$ for $\Delta=\frac{1}{2}$ and $U=1$, 1.5, 2, 3, 4, 6, 8, 12, and 16.

which characterizes a "crossover" in the ground state from nonmagnetic-like to magnetic-like properties.

B. $\langle \sigma_z^2 \rangle$

We show in Fig. 7 the local moment $\langle \sigma_z^2 \rangle$ versus $\log_2(T)$ for $\Delta = \frac{1}{2}$ and $U = 1$, 1.5, 2, 3, 4, 6, 8, 12, and 16. For comparison, we also show in Fig. 8 corresponding results for $\Delta = 0$ (i.e., no hybridization). We thus see that, for all U studied, $\langle \sigma_z^2 \rangle$ is given by the $\Delta = 0$ value down to $T \sim 10\Delta$, where it begins to drop below the $\Delta = 0$ curve. It reaches a maximum approximately at the point at which $T\chi$ joins the universal Kondo curve, and then decreases slightly at lower temperatures.

Using the perturbative expansion procedure of Ref. 17, it is simple to show that at high temperatures

$$\langle \sigma_z^2 \rangle = \frac{1}{2} + \frac{U}{4T} + O\left[\frac{1}{T^2}\right] \tag{38}$$

for any hybridization or conduction-electron band structure. Thus, a partial local moment develops for any nonzero U, in accordance with our results.

IV. MAXIMUM VALUES OF $T\chi$ AND $\langle \sigma_z^2 \rangle$

In Fig. 9 we show the maximum "effective local moment" $(T\chi)_M$ versus u^{-1}, where $u = U/\pi\Delta$, as well as the Hartree-Fock ground-state results for

$$\lim_{T \to 0} (T\chi) = (T\chi)_{GS} = [\langle n_\uparrow \rangle_{GS} - \langle n_\downarrow \rangle_{GS}]^2 . \tag{39}$$

In Fig. 10 we show the maximum local moment $\langle \sigma_z^2 \rangle_M$ versus u^{-1}, as well as the ground-state Hartree-Fock results for

$$\langle \sigma_z^2 \rangle_{GS} = \langle (n_\uparrow - n_\downarrow)^2 \rangle_{GS} . \tag{40}$$

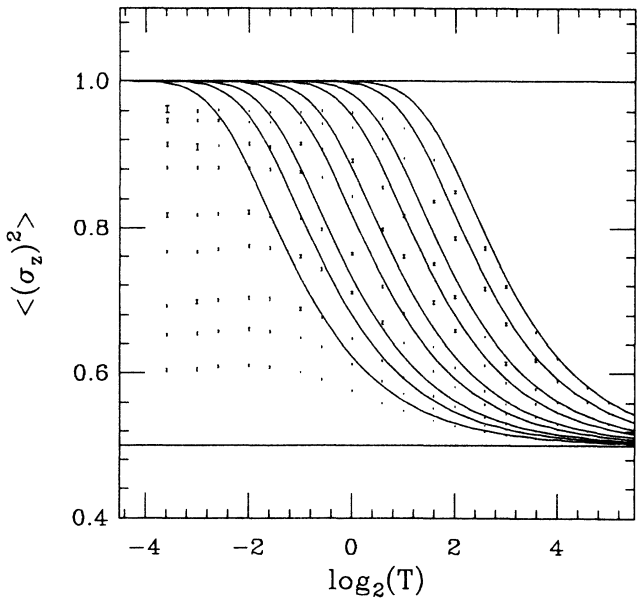

FIG. 8. Data points are the same as in Fig. 7. Solid lines are $\Delta = 0$ (i.e., no hybridization) results.

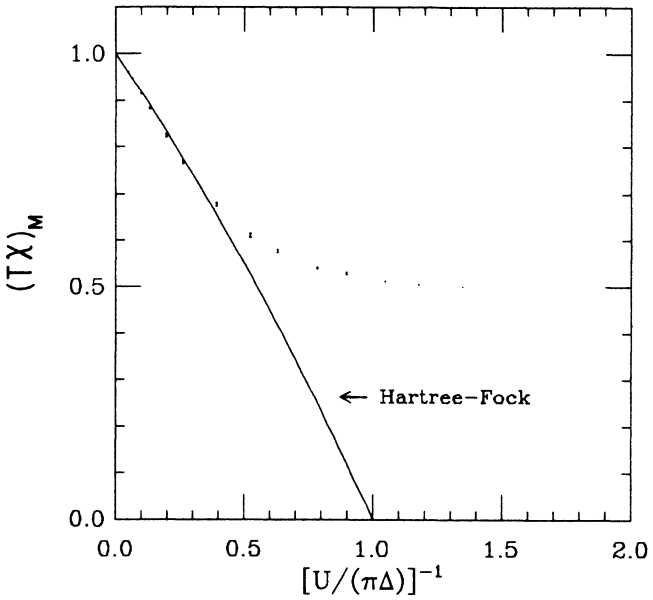

FIG. 9. Maximum value of $T\chi$ vs $[U/(\pi\Delta)]^{-1}$. Monte Carlo data points are for $\Delta = \frac{1}{2}$ and $U = 1$, $1\frac{1}{6}$, $1\frac{1}{3}$, $1\frac{1}{2}$, $1\frac{3}{4}$, 2, $2\frac{1}{2}$, 3, 4, 6, 8, 12, 16, 24, and 32. Solid line is the ground-state Hartree-Fock result.

Thus, we see that, for $u > 2$, $(T\chi)_M$ and $\langle \sigma_z^2 \rangle_M$ are well described by the Hartree-Fock ground-state predictions. Since these predictions are very close to linear in u^{-1} for $u > 2$, we thus have, to within a few percent,

$$\langle \sigma_z^2 \rangle_M \approx 1 - (0.42) u^{-1} \tag{41}$$

and

$$(T\chi)_M \approx 1 - (0.84) u^{-1} \tag{42}$$

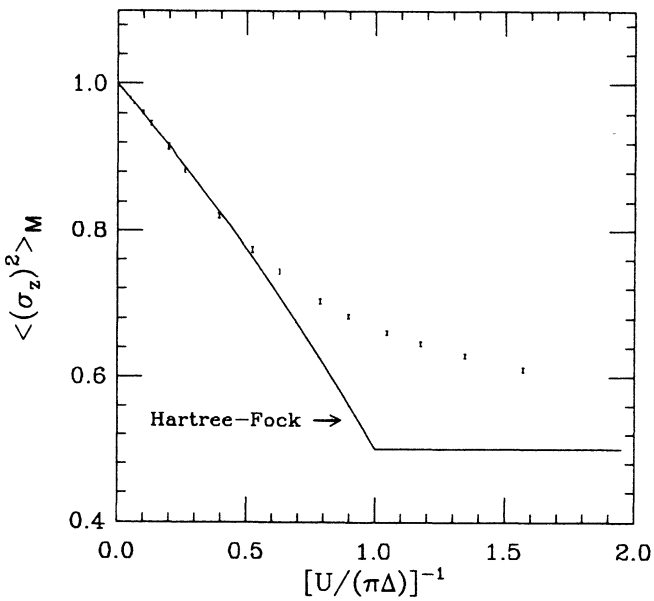

FIG. 10. Same as Fig. 9, except for $\langle \sigma_z^2 \rangle$ instead of $T\chi$.

for $u = U/\pi\Delta > 2$.

In the Hartree-Fock approximation,

$$2(1-\langle\sigma_z^2\rangle_{GS})=(1-\langle T\chi\rangle_{GS}) +[1-(\langle n_\uparrow\rangle_{GS}+\langle n_\downarrow\rangle_{GS})^2] . \quad (43)$$

Thus, in that approximation,

$$2(1-\langle\sigma_z^2\rangle_{GS})=1-\langle T\chi\rangle_{GS} \quad (44)$$

is always obeyed in the symmetric case, in analogy to Eqs. (41) and (42).

V. EFFECT OF CONDUCTION-BAND STRUCTURE ON $\langle\sigma_z^2\rangle$

Assuming V_k independent of k as before, we now consider the effect of finite conduction-electron bandwidth. The local definition of $T\chi$ that we have used, Eqs. (25) and (26), does not agree with the usual, more physical definition (total susceptibility minus susceptibility without impurity) for finite bandwidth.[18] Although the total uniform magnetic susceptibility of the system can be calculated with our algorithm and the difference taken between systems of one and no impurities, this is more time consuming. Thus we concentrate on the local moment $\langle\sigma_z^2\rangle$.

In Fig. 11 we show $\langle\sigma_z^2\rangle$ versus $\log_2(T)$ for $\pi\rho V^2=\frac{1}{2}$; $U=1.5912$; and $D=\infty$, $D=2U$, and $D=U$. (For $D=\infty$, $\pi\rho V^2=\Delta$.) The graphs merge at high temperatures, in accordance with Eq. (38). However, as the temperature is lowered, we see that the moment is enhanced by a finite conduction band.

We explain this as follows. Although both systems experience the same impurity Coulomb repulsion U, the system with finite conduction band has a smaller range of states for the impurity orbital to hybridize with. Thus, hybridization effects are reduced relative to Coulomb repulsion effects, and the moment increases.

However, as shown in Fig. 12, renormalization-group results[3] indicate that this enhancement has a very small effect on $T\chi$ for $D=2U$. (The parameters used satisfy $\sqrt{\Delta U}\sim D/4$, which may be compared with the Bethe-ansatz condition[4] for neglecting the effects of finite D, $\sqrt{\Delta U}\ll D$.) This is not true for the local definition of $T\chi$ [Eqs. (25) and (26)], as shown in Fig. 13. It is interesting that the more physical definition appears to exhibit better universal characteristics than less physical one.

In Fig. 14 we show $\langle\sigma_z^2\rangle$ versus $\log_2(T)$ for $D=1$, $\pi\rho V^2/U=\pi/16$, and varying U. This illustrates even more graphically the enhancement of $\langle\sigma_z^2\rangle$ with finite D. Presumably, if we computed $T\chi$ graphs (total susceptibility minus susceptibility without impurity) for these parameters, we would find that they first joined universal Kondo curves with increasing T_k's at increasingly higher temperatures for larger U, since $\pi\rho V^2/U$ is held constant, where the effective bandwidth cutoff D_{eff} would be given by $D_{\text{eff}}\approx(0.182)U$ for $U\le D$. However, for $U\gg D$, D_{eff} would cross over to $D_{\text{eff}}=D$,[17] and the $T\chi$ graphs would join a universal curve with the same T_k at increasingly higher temperatures.

VI. SUMMARY

Using a quantum Monte Carlo algorithm, we have performed simulations on the symmetric Anderson-magnetic-impurity model for a wide range of parameters and temperatures. We have obtained the following picture of magnetic susceptibility behavior and local-moment formation as a function of temperature, hybridi-

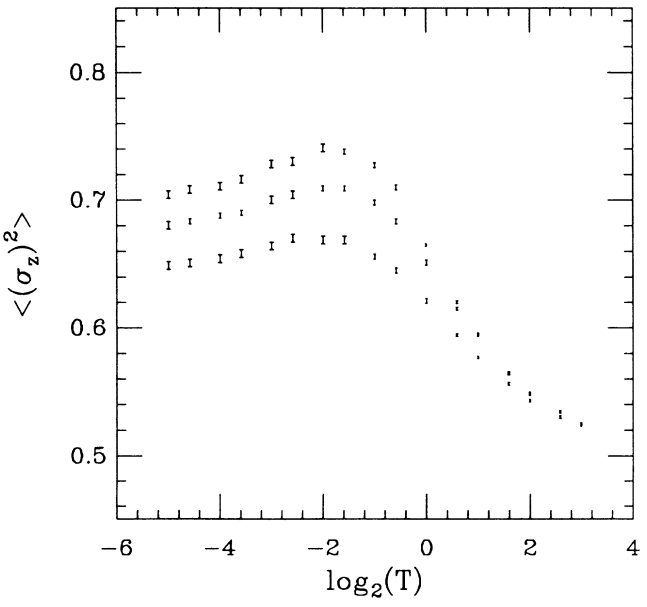

FIG. 11. $\langle\sigma_z^2\rangle$ vs $\log_2(T)$ for $\pi\rho V^2=\frac{1}{2}$ and $U=1.591$. From top to bottom, $D=U$, $D=2U$, and $D=\infty$. (For $D=\infty$, $\pi\rho V^2=\Delta$ and $U/\pi\Delta=1.013$.)

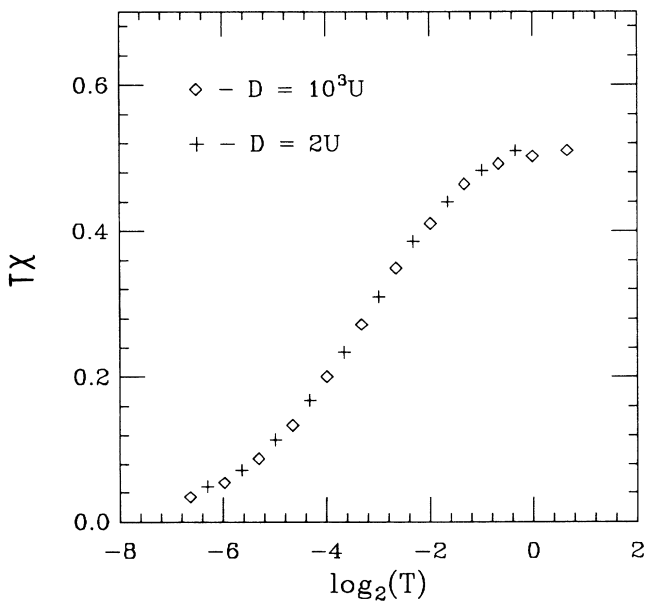

FIG. 12. $T\chi$ vs $\log_2(T)$ from Figs. 9 and 10 of Ref. 3. Data points are normalized to $\pi\rho V^2=\frac{1}{2}$ and $U=1.591$. (For $D=\infty$, $\pi\rho V^2=\Delta$ and $U/\pi\Delta=1.013$.)

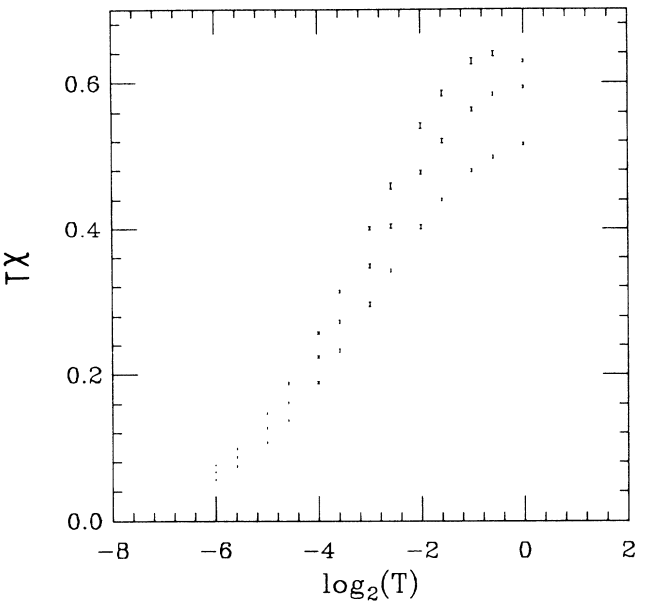

FIG. 13. Monte Carlo results for local definition of $T\chi$ vs $\log_2(T)$. $\pi\rho V^2=\frac{1}{2}$, $U=1.591$; and, from top to bottom, $D=U$, $D=2U$, and $D=\infty$.

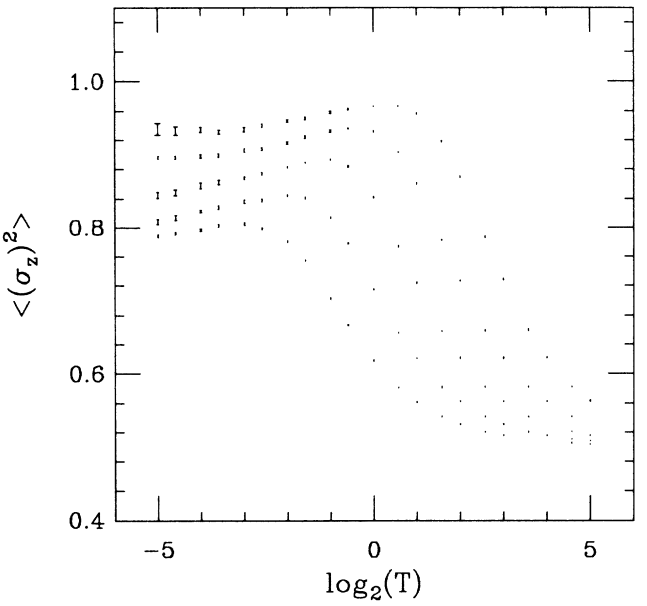

FIG. 14. $\langle\sigma_z^2\rangle$ vs $\log_2(T)$. $D=1$, $U/[\pi(\pi\rho V^2)]=16/\pi^2$, and, from top to bottom, $U=16$, 8, 4, 2, and 1.

zation width Δ, and on-site Coulomb repulsion U.

First, for the case of the flat, infinite conduction-band density of states, we find that the "effective moment" $T\chi$ is well described by the high-temperature perturbation formula[17]

$$T\chi\approx\frac{1}{2}+\frac{1}{T}\left[\frac{U}{8}-A\left[\frac{\Delta}{\pi}\right]\right]-\frac{1}{T^2}\left[AU\left[\frac{\Delta}{\pi}\right]+\frac{B}{2}\left[\frac{\Delta}{\pi}\right]^2\right], \quad (45)$$

where $A=0.853$ (Ref. 17) and $B=2.45\pm0.10$, until $T\sim20\Delta$, at which point it begins to move toward the universal Kondo curve, with T_k given by the Bethe-ansatz equations (3.1)–(3.3). For $U>2\pi\Delta$, it reaches a maximum given by

$$(T\chi)_M\approx1-(0.84)u^{-1}, \quad (46)$$

where $u=U/\pi\Delta$, and simultaneously joins the universal curve at $T_j\sim\frac{1}{4}\sqrt{\Delta U}$. For $U<2\pi\Delta$, $T\chi$ reaches a maximum before it joins the Kondo curve and, for $U\ll2\pi\Delta$, it joins the curve at $T_j\sim\frac{1}{3}\Delta$.

There is a crossover behavior when $U=(2.17)\Delta$, since $(T\chi)_M=0.5$ for $U<(2.17)\Delta$ and $(T\chi)_M>0.5$ for $U>(2.17)\Delta$. This corresponds closely to the Bethe-ansatz ground-state value $U_c=2\Delta$ marking a transition from nonmagnetic-like to magnetic-like behavior.[5]

We next find that the local moment $\langle\sigma_z^2\rangle$ is well described by the $\Delta=0$ value down to $T\sim10\Delta$ independent of U, at which time it falls below the $\Delta=0$ curve. It then reaches a maximum given for $U/\pi\Delta>2$ by

$$\langle\sigma_z^2\rangle_M\approx1-(0.42)u^{-1}, \quad (47)$$

approximately where $T\chi$ joins the universal curve, and decreases slightly at lower temperature.

Lastly, we considered a finite conduction-electron bandwidth and found that the moment $\langle\sigma_z^2\rangle$ was enhanced. We explained this as due to decreased hybridization effects, but noted that renormalization-group results indicated that $T\chi$ was much less affected than $\langle\sigma_z^2\rangle$.

ACKNOWLEDGMENTS

This work was supported by the National Science Foundation under Grant No. DMR-85-17756, and by the Cray Research Corporation and AT&T Bell Laboratories. Computations were performed at the Cray Research X-MP Computer of the San Diego Supercomputer Center.

[1]P. W. Anderson, Phys. Rev. **124**, 41 (1961).
[2]J. R. Schrieffer and P. A. Wolff, Phys. Rev. **149**, 491 (1966).
[3]H. R. Krishna-Murthy, J. W. Wilkins, and K. G. Wilson, Phys. Rev. B **21**, 1003 (1980).
[4]A. M. Tsvelick and P. B. Wiegmann, J. Phys. C **16**, 2281 (1982).
[5]A. M. Tsvelick and P. B. Wiegmann, Adv. Phys. **32**, 453 (1983), and references therein.
[6]A. Okiji and M. Kawakami, J. Appl. Phys. **55**, 1931 (1984), and references therein.

[7]J. E. Hirsch and R. M. Fye, Phys. Rev. Lett. **56**, 2521 (1986).
[8]R. Blankenbecler, D. J. Scalapino, and R. L. Sugar, Phys. Rev. D **24**, 2278 (1981).
[9]H. F. Trotter, Proc. Am. Math. Soc. **10**, 545 (1959).
[10]J. E. Hirsch, Phys. Rev. B **28**, 4059 (1983).
[11]R. M. Fye, Phys. Rev. B **33**, 6271 (1986).
[12]R. M. Fye and R. T. Scalettar, Phys. Rev. B **36**, 3833 (1987).
[13]R. M. Fye, J. E. Hirsch, and D. J. Scalpino, Phys. Rev. B **35**, 4901 (1987).
[14]J. E. Gubernatis, J. E. Hirsch, and D. J. Scalpino, Phys. Rev. B **35**, 8478 (1987).
[15]K. G. Wilson, Rev. Mod. Phys. **47**, 773 (1975).
[16]B. Horvatic and V. Zlatic, J. Phys. (Paris) **46**, 1459 (1985).
[17]F. D. M. Haldane, J. Phys. C **11**, 5015 (1978).
[18]This follows, for example, from the fact that the conduction-electron propagator in Eq. (14) of Ref. 17 is independent of magnetic field for $D=\infty$ but not for $D\neq\infty$. The Anderson-Clogston compensation theorem [P.W. Anderson and A.M. Clogston, Bull. Am. Phys. Soc. **6**, 124 (1961); P.W. Anderson, Phys. Rev. **124**, 41 (1961)] at finite temperature can also follow from this consideration.